PHYSICAL REVIEW FLUIDS **3**, 063201 (2018)

Role of hydrodynamic shear layer stability in driving combustion instability in a premixed propane-air backward-facing step combustor

Santosh Hemchandra[*]
Department of Aerospace Engineering, Indian Institute of Science, Bangalore 560011, India

Santosh Shanbhogue, Seunghyuck Hong, and Ahmed F. Ghoniem
Department of Mechanical Engineering, Massachusetts Institute of Technology, 77 Massachusetts Avenue, Cambridge, Massachusetts 02139, USA

(Received 27 August 2017; published 18 June 2018)

This paper presents a global hydrodynamic stability analysis of flow fields in a backward-facing step combustor, assuming weakly nonparallel flow. The baseline experiments in a "long" combustor of length of 5.0 m shows the presence of two combustion instability states characterized by coherent low- and high-amplitude acoustic pressure oscillations. The analysis is performed for propane-air mixtures at three values of $\phi = 0.63$, 0.72, and 0.85, which correspond to quiet, low-amplitude and high-amplitude instability states in the long combustor experiments. Base flow velocity and density fields for the hydrodynamic stability analysis are determined from time-averaged particle image velocimetry measurements made after the length of the duct downstream of the step has been shortened to eliminate acoustic pressure oscillations. The analysis shows that the shear layer mode is self-excited for the $\phi = 0.72$ case with an oscillation frequency close to that of the long combustor's fundamental acoustic mode. We show from an analysis of the weakly forced, variable density Navier-Stokes equations that self-excited hydrodynamic modes can be weakly receptive to forcing—suggesting that the low-amplitude instability in the long combustor is due to semi-open loop forcing of heat-release oscillations by the shear layer mode. At $\phi = 0.85$, the analysis shows that the flow is hydrodynamically globally stable but locally convectively unstable. Spatial amplification of velocity disturbances by the convectively unstable flow causes high-amplitude combustion instability in the long combustor case. These results show that combustion instability can be sustained by two different mechanisms by which acoustic and hydrodynamic modes being either strongly coupled result in fully closed loop forcing, or weakly coupled result in semi-open loop forcing of the flame by a self-excited hydrodynamic mode.

DOI: 10.1103/PhysRevFluids.3.063201

I. INTRODUCTION

We investigate the role of coupling between acoustic modes and hydrodynamic modes in causing combustion instability in lean premixed combustors. Flows in practical gas turbine combustors are composed of shear layers and recirculation zones, which arise from combustor design strategies adopted to achieve good fuel-air mixing and flame stabilization. These features can cause hydrodynamic instabilities. The resulting velocity oscillations often interact with the premixed flame sheet, causing it to wrinkle and distort, leading to heat-release oscillations that can potentially drive acoustic pressure oscillations in the combustor [1]. The importance of the role of hydrodynamic

---

[*] hsantosh@aero.iisc.ernet.in

fluctuations in driving the flame response has been recognized in prior fundamental studies on heat-release response characteristics of premixed flames (see, e.g., Refs. [2–4]) and combustor stability margins [5,6]. Thus, insight into how acoustic oscillations and hydrodynamic instability modes couple, resulting in heat-release oscillations, is key to understanding the conditions under which combustion instability may occur in gas turbine combustors.

In this paper, we perform a nonlinear analysis of the forced, variable density Navier-Stokes equations using the method of multiple scales to gain physical insight into possible mechanisms by which hydrodynamic modes of the flow can be excited by system acoustic modes leading to the onset of combustion instability. Hence, we assume that acoustic forcing amplitudes are small compared to the magnitudes of the hydrodynamic flow velocity response. A solution to leading order in forcing amplitude, for the early evolution of contributions from individual hydrodynamic modes to the flow response, is derived. This solution shows that unstable, self-excited hydrodynamic modes dominate the flow response through their natural dynamics, while stable hydrodynamic modes can be driven by the forcing imposed by the acoustic field, if they are forced in regions of high receptivity. The results also identify formally the factors influencing the receptivity of hydrodynamic modes to imposed forcing.

Sufficiently large regions of locally absolutely unstable flow profiles along the streamwise direction can result in hydrodynamic modes becoming globally self-excited [7,8]. Prior local [9–13] and global [14] stability analyses have shown that the presence of shear layers and recirculation zones can result in regions of local absolute instability in combustor flows. Further, flame-induced density gradients can stabilize locally absolutely unstable regions (see, e.g., Refs [9–12,15] for recent studies), resulting in nominally unstable hydrodynamic modes becoming marginally unstable or even stable globally, while still being locally convectively unstable [7,8]. These stable modes can behave like disturbance amplifiers, leading to large amplitude velocity response when forced by acoustic oscillations. As such, these possibilities suggest two possible mechanisms by which coherent velocity oscillations and hence, heat-release oscillations, can be sustained in lean premixed combustors as described next.

Figure 1(a) shows schematically the mechanism that can cause combustion instability when self-excited hydrodynamic modes are present. These modes cause flow oscillations at their characteristic *hydrodynamic* eigenfrequency, f_H, which in turn interact with the premixed flame sheet, causing heat-release oscillations with frequency f_H. These heat-release oscillations can then result in acoustic pressure oscillations in the combustor if the Rayleigh-criterion is satisfied, i.e., positive coupling between the pressure and heat-release oscillations and weak acoustic damping. The former condition is more likely to be true in general when $f_H \sim f_a$ where f_a is the acoustic eigenfrequency corresponding to one of the acoustic eigenmodes of the combustor. As f_a and f_H become progressively different, i.e., the forcing is more nonresonant, the acoustic pressure oscillation amplitudes become progressively smaller. Thus, the key process sustaining heat-release oscillations and hence, acoustic pressure oscillations, for the mechanism shown in Fig. 1(a), is the hydrodynamically self-excited nature of the flow field and not the effect of acoustic feedback on the hydrodynamic oscillations. Therefore, we call the mechanism shown in Fig. 1(a) the semi-open loop mechanism.

Figure 1(b) shows the possibility when hydrodynamic modes are either self-excited and synchronize with acoustic oscillations or are naturally stable and excited by the acoustic field. In both scenarios, the hydrodynamic field responds strongly to the imposed acoustic field, resulting in high amplitude velocity oscillations at the oscillation frequency of the acoustic field. These in turn can result in heat-release oscillations due to the interaction between velocity oscillations and the flame sheet. Therefore, if these heat-release oscillations and the acoustic pressure field satisfy Rayleigh's criterion and acoustic damping losses are small, sustained acoustic pressure oscillations can be established in the combustor. Since both of these conditions would be best satisfied nominally by the combustor acoustic eigenmodes, strong acoustic oscillations at the corresponding acoustic eigenfrequencies would result. We call this mechanism the "fully closed loop" mechanism because the

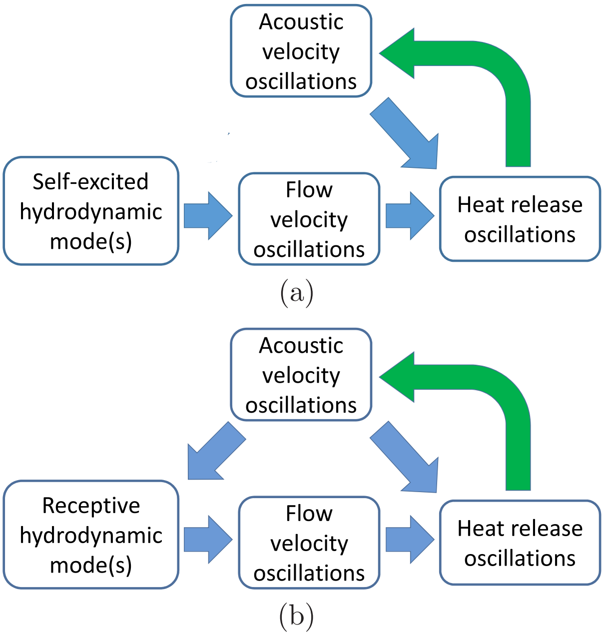

FIG. 1. Fundamental mechanisms though which hydrodynamic instability modes and acoustic modes can couple during combustion instability: (a) semi-open loop, (b) fully closed loop.

key process sustaining heat-release oscillations is the excitation of hydrodynamic velocity oscillations by the acoustic field.

In this paper, we show evidence for the above mechanisms in a backward-facing step combustor. Combustion instabilities in the backward-facing step geometries have been examined by several other studies in the past [16,17]. These prior studies have highlighted the role of vortex shedding at the step due to shear layer rollup as being an important driving mechanism for combustion instability in these combustors. In the present study, we consider the recent premixed propane-air backward-facing step combustor experiments of Hong *et al.* [18,19]. We consider three cases corresponding to equivalence ratios of $\phi = 0.63$, 0.72, and 0.85 from the database of Hong *et al.* [18]. The first case does not show combustion instability. The latter two cases show two *different* states of combustion instability, characterized by different oscillation amplitudes and unsteady flame behavior [18]. These experiments were repeated by the same group [19] with a shortened overall combustor length downstream of the step. This resulted in stable combustor operation over the entire ϕ range for which combustion instability was observed in the former setup [18].

We determine the global hydrodynamic instability modes as well as their corresponding adjoint modes at $\phi = 0.63$, 0.72, and 0.85, using the techniques for weakly nonparallel flow developed by Juniper and Pier [20]. Time-averaged velocity and density fields determined from high-speed particle image velocimetry (PIV) measurements in the short combustor experiments are used as base flows for these analyses. The linear stability analysis shows that the global shear layer mode in the combustor is unstable for the $\phi = 0.63$ and 0.72 cases, with oscillation frequencies $\sim$85 Hz and $\sim$42 Hz, respectively. The latter is close to the fundamental combustor acoustic eigenfrequency of $\sim$40 Hz, as estimated from an acoustic network analysis that accounts for spatially varying mean temperature in the combustor [21]. This suggests that the acoustic oscillations in the $\phi = 0.72$ case are sustained by the self-excited shear layer mode through the the semi-open loop mechanism, whereas the acoustic oscillations excited by the $\phi = 0.63$ case would be strongly nonresonant due to the significant difference between the combustor acoustic eigenfrequency and the shear layer oscillation frequency resulting in the combustor being stable.

In contrast, the shear layer mode at $\phi = 0.85$ is shown to be globally stable and, more importantly, the corresponding adjoint velocity modes [22] show that this mode is receptive to forcing near the step. This suggests that the fully closed loop mechanism [see Fig. 1(b)] drives acoustic pressure oscillations for $\phi = 0.85$ at the fundamental acoustic eigenfrequency of the long combustor. As such, the analysis in this paper suggests that the fundamentally different combustion instability states observed in the long combustor experiments [18] are due to differences in the way hydrodynamic modes and acoustic oscillations couple.

Qualitative evidence of semi-open loop forcing can also be found in the experiments of Chakravarthy *et al.* [23]. Their experiments vary the nominal air velocity in the combustor as a control parameter for a fixed fuel mass flow rate. With increasing air velocity in their experiments, the boundary layer thickness at the step becomes smaller and the strength of the recirculation zone increases. This results in decreasing shear layer thicknesses at the step, coupled with streamwise velocity profiles with strong regions of reverse flow. Prior local stability analyses of model flow profiles having these characteristics [9,24], as well as the analysis shown in the present paper, suggest that this would lead to the emergence of regions of local absolute instability downstream of the step. At sufficiently high air flow velocities, this results in globally self-excited shear layer oscillations, which then drive heat-release oscillations in a semi-open loop manner by coupling with the flame sheet. Chakravathy *et al.* [23] report a linear variation of the combustion instability frequency with upstream flow velocity for some of their conditions and show that this frequency is insensitive to the length of the duct downstream of the step. This suggests that a self-excited hydrodynamic instabilities drive heat-release oscillations in their combustor rather than the acoustic oscillations.

The rest of the paper is organized as follows. Section II presents details of the theoretical formulation. Section III summarizes details of the experimental setup and combustion instability characteristics observed in the prior experimental study. Section IV describes the numerical methods used. The results of the present study are discussed in Sec. V. Finally, Sec. VI concludes the paper with a discussion on the implications of the present results for combustor design.

II. THEORETICAL FORMULATION

We develop an approximate solution for the evolution of the hydrodynamic response of the flow to harmonic forcing imposed by background combustion noise in the combustor at the onset of thermoacoustic pressure oscillations. The governing equations for the hydrodynamic field are the fully nonlinear, variable density, Navier-Stokes (NS) equations in the low Mach number limit. These equations can be written symbolically in nondimensional form, using appropriately chosen length (L_{ref}), velocity (U_{ref}), and density (ρ_{ref}) scales as follows:

$$\mathbf{B}'\frac{\partial q}{\partial t} + \mathbf{N}(q,q) = \frac{1}{\mathrm{Re}}\mathbf{L}_{\mathbf{v}}(q) + \epsilon^2 F(x,y,t), \tag{1}$$

where $q = [\rho\ u\ v\ p]^T$ is the nondimensional state vector of the flow and $\mathrm{Re} = U_{\mathrm{ref}}L_{\mathrm{ref}}/\nu$, is the Reynolds number. The operators $\mathbf{N}$ and $\mathbf{L}_{\mathbf{v}}$ represent inviscid and viscous terms, respectively. The matrix $\mathbf{B}'$ is a diagonal matrix with diagonal elements $\{1,\rho,\rho,0\}$. The vector $F = [f_m\ f_u\ f_v\ f_e]^T$ represents forcing terms due to unsteady mass, momentum, and energy addition/removal into the flow, written in nondimensional form. During the early stages of thermoacoustic instability, the amplitudes of the acoustic velocity oscillations are small compared to the amplitude of velocity oscillations associated with the hydrodynamic response of the flow. Therefore, we make a weakly forced flow assumption in Eq. (1) and assume that the amplitude of the forcing is $O(\epsilon^2)$, where ϵ is the amplitude of the leading order hydrodynamic flow response. Equation (1) is complemented by no-slip, adiabatic conditions at walls and the following initial condition:

$$q(x,y,0) = Q_o(x,y), \tag{2}$$

where $Q_o = [\rho_o\, U_o\, V_o\, P_o]^T$ is the base flow state around which perturbations evolve. Following the method of multiple scales [25], we assume that the evolution of the flow is characterized by variations on a fast and a slow timescale whose ratio is given by ϵ. Thus, assuming q and F depend on independent "fast": $t_1 = t$ and "slow": $t_2 = \varepsilon t$ time variables, Eq. (1) can be rewritten as follows:

$$\mathbf{B}'\frac{\partial q}{\partial t_1} + \epsilon \mathbf{B}'\frac{\partial q}{\partial t_2} + \mathbf{N}(q,q) = \frac{1}{\mathrm{Re}}\mathbf{L_v}(q) + \epsilon^2 F(x,y,t_1). \tag{3}$$

Next, we expand q in terms of an asymptotic series in ε as follows:

$$q(x,y,t_1,t_2) = Q_o(x,y) + \epsilon q_1(x,y,t_1,t_2) + \epsilon^2 q_2(x,y,t_1,t_2) + \cdots \tag{4}$$

Using this expansion in Eq. (3) yields at $O(1)$, the system of steady NS equations for Q_o. At $O(\epsilon)$, the system of unsteady linearized Navier-Stokes (LNS) equations is obtained for q_1 as follows:

$$\mathbf{B}\frac{\partial q_1}{\partial t_1} + \mathbf{L}(q_1; Q_o) = 0, \tag{5}$$

where the operator $\mathbf{L}$ represents the spatial derivative terms arising from $\mathbf{N}$ and $\mathbf{L_v}$ that are linear in q_1 and the matrix $\mathbf{B}$ is a diagonal matrix with diagonal elements $\{1,\rho_o,\rho_o,0\}$. The solutions to Eq. (5) are determined by a linear combination of eigensolutions of the form $q_{1m}(x,y,t_1) = \tilde{q}_{1m}(x,y)e^{-i\omega_{gm}t_1}$, i.e., the *global* hydrodynamic instability modes which, from Eq. (5), satisfy the following linear eigenvalue problem:

$$-i\omega_{gm}\mathbf{B}\tilde{q}_{1m} + \mathbf{L}(\tilde{q}_{1m}; Q_o) = 0, \tag{6}$$

where the real part of ω_{gm} [Real(ω_{gm})] is the normalized oscillation frequency and the imaginary part [Imag(ω_{gm})] is the temporal growth rate of the hydrodynamic mode. Hence, using complex valued notation, the solution for $q_1(x,y,t_1,t_2)$ can be written as follows:

$$q_1(x,y,t_1,t_2) = \sum_{m=0}^{M} \mathrm{Real}(A_m(t_2)\tilde{q}_{1m}(x,y)e^{-i\omega_{gm}t_1}), \tag{7}$$

where $A_m(t_2)$ are the slowly varying amplitudes that quantify the contribution of each linear eigenmode to the leading order flow response and M is the number of global instability modes. We will refer to $\tilde{q}_{1m}$ and Eq. (6) as the "direct" instability modes and the "direct" instability problem, respectively, in the rest of this paper.

An equation for $A_m(t_2)$ in Eq. (7) can be derived from the equations at $O(\epsilon^2)$, which can be written as follows:

$$\mathbf{B}\frac{\partial q_2}{\partial t_1} + \mathbf{L}(q_2; Q_o) = -\frac{\partial q_1}{\partial t_2} + \mathbf{N_1}(Q_o,q_1) + F(x,y,t_1), \tag{8}$$

where the operator $\mathbf{N_1}$ represents the contributions from $\mathbf{N}(q,q)$ in Eq. (3), which are second degree in q_1. The contribution from the second term on the right in Eq. (8) is small when compared to the third term during the early evolution of the flow response, i.e., for $t_2 \ll 1$. This is because $|A_m(t_2)| \ll 1$ for $t_2 \ll 1$ and hence $\mathbf{N_1}(q_1,Q_o) \sim O(|A_m|^2)$ would be small with respect to the third term on the right-hand side of Eq. (8), which is $O(1)$. Hence, neglecting nonlinear terms in Eq. (8), yields the following equation for the early evolution of q_2:

$$\mathbf{B}\frac{\partial q_2}{\partial t_1} + \mathbf{L}(q_2; Q_o) = -\frac{\partial q_1}{\partial t_2} + F(x,y,t_1). \tag{9}$$

The prior asymptotic analyses of the compressible NS equations performed by Mariappan and Sujith [26] and Moeck *et al.* [27] showed that the acoustic field imposes a global acceleration on the hydrodynamic field. Therefore, we choose $F(x,y,t_1) = -i\omega_a\rho_u\tilde{q}_a(x,y)e^{-i\omega_a t_1}$, where $\tilde{q}_a(x,y) = [0\ \tilde{u}_a(x,y)\ \tilde{v}_a(x,y)\ 0]^T$ is the acoustic eigenmode, ω_a is the acoustic eigenfrequency, and ρ_u is the unburnt gas density. In practical combustors, a potential source for this sort of forcing is the combustion noise generated at the acoustic eigenfrequency by broadband background turbulent velocity fluctuations coupling with the flame sheet.

Thus, setting $q_2(x,y,t_1,t_2) = \tilde{q}_2(x,y,t_2)\exp(-i\omega_a t_1)$ and using Eq. (7) in Eq. (9) yields

$$-i\omega_a \mathbf{B}\tilde{q}_2 + \mathbf{L}(\tilde{q}_2; Q_o) = -\sum_{m=0}^{M}\left[e^{i(\omega_a-\omega_{gm})t_1}\frac{dA_m}{dt_2}\mathbf{B}\tilde{q}_{1m}(x,y)\right] - i\omega_a\rho_u\tilde{q}_a(x,y). \tag{10}$$

Assuming $\omega_a = \omega_{gm} + \epsilon\Omega_m$, Eq. (10) yields

$$-i\omega_a \mathbf{B}\tilde{q}_2 + \mathbf{L}(\tilde{q}_2; Q_o) = -\sum_{m=0}^{M}\left[e^{i\Omega_m t_2}\frac{dA_m}{dt_2}\mathbf{B}\tilde{q}_{1m}(x,y)\right] - i\omega_a\rho_u\tilde{q}_a(x,y). \tag{11}$$

Since the right side of Eq. (11) is a function of space alone, bounded solutions for $\tilde{q}_2$ exist only if the terms on the right-hand side of Eq. (11) are orthogonal to the adjoint modes of the operator on the left, i.e., the adjoint modes of the unsteady LNS equations with respect to a suitably defined inner product. Here, we define this inner product between two flow states q_i and q_j as follows:

$$\langle q_i, q_j\rangle = \int_0^{L_x}\int_{-h}^{h} q_i^H \mathbf{P} q_j \, dy\, dx, \tag{12}$$

where the matrix $\mathbf{P}$ is a diagonal matrix whose diagonal elements are: $\{1,\rho_o,\rho_o,1\}$ and the superscript "H" represents the conjugate transpose. The limits of integration in Eq. (12) represent the streamwise and transverse extents of the flow domain of interest.

Thus, adjoint modes $q_1^\dagger(x,y,t_1) = \tilde{q}_1^\dagger(x,y)e^{i\omega_g^\dagger t_1}$, corresponding to the direct stability modes, can be determined by solving the following adjoint stability equation,

$$i\omega_g^\dagger \mathbf{B}^\dagger \tilde{q}_1^\dagger + \mathbf{L}^\dagger(\tilde{q}_1^\dagger; Q_o) = 0, \tag{13}$$

where $\tilde{q}_1^\dagger = [\tilde{\rho}_1^\dagger \tilde{u}_1^\dagger \tilde{v}_1^\dagger \tilde{p}_1^\dagger]^T$. The matrix $\mathbf{B}^\dagger$ and adjoint operator $\mathbf{L}^\dagger$ are defined such that $\tilde{q}_{1m}^\dagger$ and $\omega_{gm}^\dagger$ satisfy the following condition:

$$\langle \tilde{q}_{1m}^\dagger, -i\omega_{gm}\mathbf{B}\tilde{q}_{1m} + \mathbf{L}(\tilde{q}_{1m}, Q_o)\rangle = \langle i\omega_{gm}^\dagger \mathbf{B}^\dagger\tilde{q}_{1m}^\dagger + \mathbf{L}^\dagger(\tilde{q}_{1m}^\dagger; Q_o), \tilde{q}_{1m}\rangle. \tag{14}$$

It can be shown using Eqs. (6), (13), and (14) that $\omega_{gm}^\dagger = \omega_{gm}^*$, where the superscript * denotes the complex conjugate and that $\tilde{q}_{1m}$ and $\tilde{q}_{1m}^\dagger$ satisfy a biorthogonality condition as follows [28]:

$$\langle \tilde{q}_{1m}^\dagger, \mathbf{B}\tilde{q}_{1n}\rangle = C\delta_{mn}, \tag{15}$$

where C is a constant that depends on the normalization applied to the direct and adjoint modes and δ_{mn} is the Kronecker δ.

Thus, using the inner product [Eq. (12)] and the biorthogonality property [Eq. (15)] and requiring that the expression on the right-hand side of Eq. (11) be orthogonal to each of the adjoint modes yields an equation for the modal amplitudes, $A_m(t_2)$, as follows:

$$\frac{dA_m}{dt_2} = -i\omega_a\rho_u\frac{\langle \tilde{q}_{1m}^\dagger, \tilde{q}_a\rangle}{\langle \tilde{q}_{1m}^\dagger, \mathbf{B}\tilde{q}_{1m}\rangle}e^{-i\Omega_m t_2}. \tag{16}$$

In addition, Eq. (2) yields $A_m(0) = 0$. Thus, integrating Eq. (16) yields the following solution for $A_m(t_2)$:

$$A_m(t_2) = \frac{\omega_a\rho_u\langle \tilde{q}_{1m}^\dagger, \tilde{q}_a\rangle}{\Omega_m\langle \tilde{q}_{1m}^\dagger, \mathbf{B}\tilde{q}_{1m}\rangle}[e^{-i\Omega_m t_2} - 1]. \tag{17}$$

Using the above result, the early-stage evolution of the leading-order contribution to the unsteady flow response [i.e., q_1 in Eq. (4)] in terms of the original temporal variable, t, can be written as follows:

$$q_1(x,y,t) = \omega_a \rho_u \sum_{m=0}^{M} R_m[q_{1m}; q_a] \tilde{q}_{1m}(x,y)\{e^{-i\omega_a t} - e^{-i\omega_{gm} t}\}, \tag{18}$$

where the functional $R_m[q_{1m}; q_a]$ can be written in terms of $\tilde{q}_{1m}^{\dagger}$ and $\tilde{q}_a$ as follows:

$$R_m[q_{1m}; q_a] = \frac{\langle \tilde{q}_{1m}^{\dagger}, \tilde{q}_a \rangle}{\Omega_m \langle \tilde{q}_{1m}^{\dagger}, \mathbf{B}\tilde{q}_{1m} \rangle}. \tag{19}$$

The term in the braces of Eq. (18) now determines whether the flow responds directly to forcing or the natural self-excited dynamics dominate. If one or more of the global hydrodynamic modes are unstable, then the $e^{-i\omega_{gm} t}$ term in Eq. (19) is dominant and the subsequent evolution of the flow is controlled by its self-excited dynamics. If the global hydrodynamic modes are stable, then the $e^{-i\omega_{gm} t}$ decays, resulting in the forced response of the flow at the excitation frequency ω_a dominating the response. In both cases $R_m[q_{1m}; q_a]$ controls the extent to which a given hydrodynamic mode contributes to the overall unsteady flow oscillation, i.e., its *receptivity*. The inner product in the numerator in Eq. (19) quantifies the efficiency with which the imposed excitation overlaps with the adjoint mode. As such, the adjoint mode quantifies the local receptivity of the mode to forcing as has been discussed in other studies (see, e.g., Ref. [29]). The inner product in the denominator in Eq. 19 quantifies the degree of "nonnormality," i.e., how dissimilar the direct mode is from its adjoint. Locally convectively unstable flows in general show higher levels of nonnormality and would hence be more receptive to forcing as Eq. (19) suggests.

The quantity Ω_m quantifies the extent of detuning between the hydrodynamic eigenfrequency and the imposed acoustic oscillation. Thus, from Eq. (19) it is clear that globally stable hydrodynamic modes, whose eigenfrequencies are very different from that of the imposed forcing, contribute very little to the evolution of the flow. Observations supporting these results have been reported in other prior experimental studies of other flow configurations. For example, Schadow and Gutmark [17] describe the sensitivity of the response of an acoustically forced, nominally isothermal turbulent jet. They show experimentally that these jets show rapid shear layer rollup and resultant high amplitude velocity oscillations at the end of the potential core, at a preferred excitation frequency that scales linearly with the nominal jet centerline velocity. Since isothermal jets have velocity profiles that are convectively unstable everywhere, the associated global hydrodynamic eigenmodes are temporally stable. Hence, Eq. (19) suggests that the preferred excitation frequency reported by Schadow and Gutmark [17] corresponds to that for which the forcing frequency matches the natural oscillation frequency of the shear layer instability mode (i.e., $|\Omega_m| \rightarrow 0$).

Thus, the above result suggests that, if unstable hydrodynamic modes do not couple with the imposed forcing during the evolution of the flow beyond the early stage due to nonlinearity becoming significant, they would only drive acoustic pressure oscillations by generating coherent heat-release oscillations at their eigenfrequencies, resulting in semi-open loop forcing. However, if they do synchronize with the imposed forcing, strong oscillations at the acoustic eigenfrequencies of the combustor can result. Likewise, if hydrodynamic modes are stable, the flow dynamics is driven by their response to the forcing imposed by the acoustic field. Both these scenarios can result in fully coupled forcing of acoustic oscillations in the combustor. Note that, in the latter case, whether heat-release oscillations generated by the initial evolution of instabilities can eventually grow into sustained limit cycle oscillations is still governed by the classic Rayleigh criterion connecting pressure and heat-release oscillations.

We use the insight gained from the above analysis to understand the mechanisms underlying the two states of combustion instability observed in the experiments of Hong *et al.* [19].

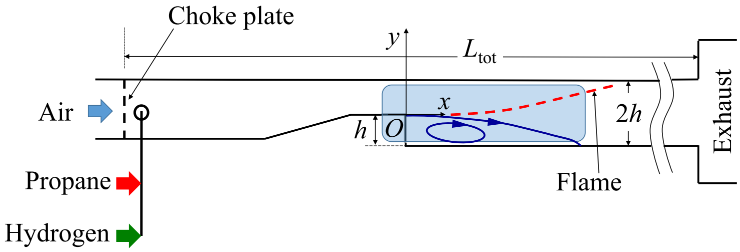

FIG. 2. Schematic of experimental setup.

III. EXPERIMENTAL STUDY

We briefly describe the experiments performed by Ghoniem and coworkers [18,19] that are pertinent to understanding the results of the analysis described in this paper, while referring the reader to the original papers for additional details regarding the instrumentation, measurement, and post-processing techniques adopted in the experiments. Figure 2 shows a schematic layout of the experimental setup. The combustor is a stainless steel duct with a rectangular cross-section 0.16 m wide and 0.04 m high. The upstream air inlet is choked and a ramp starting 0.45 m from this location reduces the channel height to 0.02 m over a length of 0.15 m. This is followed by a constant area section for a length of 0.4 m, after which a step returns the channel height abruptly to 0.04 m. The fuel mixture, composed of propane and hydrogen in varying proportions by volume, is injected 0.02 m downstream of the choke plate. This was found sufficient to ensure that oscillations in the equivalence ratio, ϕ, at the step were negligibly small [18].

Experiments were performed at upstream preheat temperatures of 300, 400, and 500 K and propane-hydrogen ratios of 50:50, 70:30, and 100:0 by volume. The flow Reynolds number, Re, based on step height and area-averaged inflow velocity at the step was maintained at 6500 in all cases. For each value of the upstream temperature and fuel composition, the overall ϕ was varied as a control parameter from the lean blow-out limit toward 1.0 using separate, calibrated mass flow controllers on the hydrogen and propane lines. The net inlet velocity at the step changed by less than 10% across all cases. These experiments were performed for two combustor lengths: $L_{\text{tot}} = 5.0$ m ("long") [18] and 1.5 m ("short") [19] (see Fig. 2), by changing the length of the section between the step and the combustor exit. In both the long and short combustor experiments, acoustic pressure measurements were taken at various locations along the axial length of the combustor. Time-resolved flow-field measurements near the step were obtained using PIV [18,19].

Hong *et al.* [18] present a detailed experimental characterization of the various combustion instability states and flow-field characteristics observed in the long combustor experiments. Figure 3 shows the variation of the overall sound pressure level (OASPL) measured in the long (black crosses) and short (red "+") combustor experiments, as a function of ϕ for the case of propane-air at a preheat temperature of 300 K. Consider first the long combustor case. No discernible coherent pressure oscillations are observed for $\phi < 0.68$. Increasing ϕ further leads to the emergence of coherent acoustic pressure oscillations with an OASPL of ≈140–150 dB accompanied by wrinkling of the flame sheet attached near the step due to shear layer rollup. When $\phi > 0.8$, coherent acoustic pressure oscillations with an OASPL of 160 dB are observed. Following Hong *et al.* [18] these three states are designated as "Mode I," "Mode II," and "Mode III," respectively. The frequency at which peak pressure oscillation amplitudes were observed was 40 Hz for the Mode III state. The corresponding results for the Mode II state showed an oscillation frequency ∼40 Hz with some variability over ϕ. The value of 40 Hz corresponds to the fundamental acoustic eigenfrequency of the long combustor as determined from an acoustic network analysis [21].

The qualitative dynamic behavior of the flame in each of these states is described using time-resolved flame luminosity images in Hong *et al.* [21]. These images show that the flame surface nominally remains largely attached near the step in Mode II while being wrinkled by the passage of

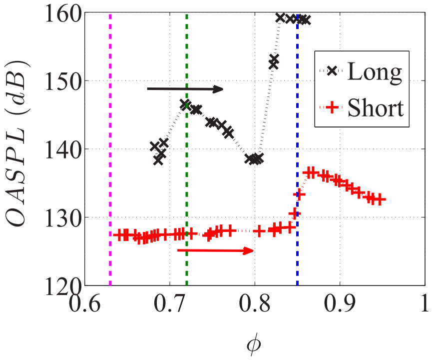

FIG. 3. Variation of overall sound pressure level with varying ϕ for the propane-air case. The broken vertical lines are at the values of ϕ analyzed in this paper. The arrows show the direction in which ϕ was varied in each case. Figure adapted from data presented in Refs. [18,19].

shear layer rollup induced vortices. The Mode III state is characterized by larger amplitude flame motions involving periodic flame flame flashback and re-attachment at the step.

We focus our stability analysis in this paper on the short combustor, propane-air cases corresponding to $\phi = 0.63$, 0.72, and 0.85, all at a preheat temperature of 300 K. Figure 3 shows that these cases correspond to the operating states in Modes I, II, and III, respectively, for the long combustor. However, the cases at the corresponding operating conditions in the short combustor do not show the presence of coherent acoustic pressure oscillations [19]. The acoustic pressure oscillations are eliminated experimentally by reducing the length of the combustor downstream of the step to realize the "short" combustor, without changing any details of the flow conditioning and geometry of the combustor duct upstream of the step. Thus, the time-averaged flow fields from PIV measurements in the short combustor represent the base flow state from which onset of combustion instability happens in the long combustor at corresponding nominal inflow conditions. Hence, we use time-averaged flow fields from the short combustor PIV measurements [19], as described in the next section, to determine base flow velocity and density profiles that are then used to determine the various terms in Eq. (19) from a hydrodynamic stability analysis performed using methods described in the next section.

IV. NUMERICAL METHODS

A. Direct and adjoint global modes

Prior stability analysis studies of weakly nonparallel flows [7,8,30] using the method of Wentzel-Kramers-Brillouin-Jeffreys (WKBJ) expansion have shown that direct global modes can be constructed from series of local parallel-flow stability analyses using flow profiles at successive streamwise locations of the nonparallel flow. Recently, these methods have been used to determine global instability mode characteristics of wakes [20,31] and jets [32]. We refer the reader to the recent paper of Juniper and Pier [20] for the complete mathematical formulation and limit the discussion here to an overview. In all the discussion that follows, all lengths and velocities are normalized by the step height (h) (see Fig. 2) and the area-averaged flow velocity at the step. The unburnt gas density is chosen as the reference density. The origin of the coordinate system is taken to be the edge of the step.

The direct global modes and eigenvalues are determined by solving Eq. (6) along with no-slip and adiabatic wall boundary conditions and assuming $|\tilde{q}_{1m}(x,y)| \rightarrow 0$ as $x \rightarrow \pm\infty$ (open flow). The global mode $\tilde{q}_{1m}(x,y)$ can be written as follows [7,8,20,31]:

$$\tilde{q}_{1m}(x,y) = \hat{q}^{\pm}_{1m}(y;x,\omega_g)\exp\left[i\int_{x_c}^{x} k^{\pm}(x';\omega_g m)dx'\right], \tag{20}$$

where the functions $\hat{q}^{\pm}_{1m}(y;x,\omega_g)$ and $k^{\pm}(x;\omega_g)$ are determined from the local direct parallel flow spatial stability problem at each streamwise location x, using local U_o and ρ_o profiles [7,8]. The local direct stability problem for $\hat{q}_{1m}$ is obtained by neglecting streamwise derivatives of base flow quantities in the operator $\mathbf{L}$ in Eq. (5) and assuming a normal-mode form for q_{1m} as $q_{1m}(x,y,t) = \hat{q}_{1m}(y)e^{i(kx-\omega t)}$, where k and ω are the local spatial and temporal eigenvalues, respectively. Thus, the $\hat{q}^{\pm}_{1m}$ and $k^{\pm}$ in Eq. (20) are determined by solving the local eigenvalue problem for k assuming $\omega = \omega_{gm}$. This process yields two solutions for the eigenvalue $k^{\pm}$ and the corresponding local spatial eigenvectors $\hat{q}^{\pm}_{1m}$ at each streamwise location.

A leading order approximation for ω_{gm} from local direct stability analysis can be determined as follows. First, the streamwise variation of the local absolute eigenvalue, $\omega = \omega_{om}$, at which $d\omega/dk = 0$ for the local parallel flow stability problem is determined. The flow is locally absolutely unstable if $\mathrm{Im}(\omega_{om}) > 0$ and convectively unstable if $\mathrm{Im}(\omega_{om}) < 0$ [33]. The estimate of the global eigenmode ω_{gm} is then determined by the value of the analytic continuation of $\omega_{om}(x)$ onto the complex x plane, at $x = x_s$, where $d\omega_{om}/dx = 0$ [7,8,34]. The point x_s is now a branch point in the complex x plane where the two $k^{\pm}(x;\omega_{gm})$ spatial eigenvalue branches, now viewed as functions of streamwise location x, meet. The corresponding branch cut intersects the real x axis at the location x_c, which is the lower limit of the integral in Eq. (20) (see Juniper and Pier [20]). Thus, the positive sign on $\hat{q}_{1m}$ and k in Eq. (20) corresponds to $x > x_c$ and the opposite for $x < x_c$.

Juniper and Pier [20] have extended the WKBJ theory for the LNS equations [Eq. (6)] to the adjoint LNS equations [Eq. (13)]. Thus, the adjoint global modes $\tilde{q}^{\dagger}_{1m}$ can be written in terms of the local adjoint spatial eigenvectors $\hat{q}^{\dagger\pm}_{1m}$ and adjoint spatial eigenvalues $k^{\dagger\pm}$ as follows:

$$\tilde{q}^{\dagger}_{1m}(x,y) = \hat{q}^{\dagger\pm}_{1m}(y;x,\omega^{\dagger}_{gm})\exp\left[i\int_{x_c}^{x} k^{\dagger\pm}(x';\omega^{\dagger}_{gm})dx'\right]. \tag{21}$$

Juniper and Pier [20] show that $k^{\dagger\pm} = k^{\mp *}$ and $\omega^{\dagger}_{gm} = \omega^{*}_{gm}$. The $\hat{q}^{\dagger\pm}_{1m}$ can be constructed by solving the local adjoint stability problem derived from Eq. (13) in the same manner as the local direct stability problem is derived from Eq. (5). The explicit form of the operator $\mathbf{L}^{\dagger}$ and the matrix $\mathbf{B}^{\dagger}$ in Eq. (13) can be derived from Eqs. (6) and (14) using integration by parts. Alternatively, the local direct stability problem derived from Eq. (6), can be numerically discretized and the local adjoint problem can then be constructed by taking the conjugate transpose of the direct problem [20,22]. We adopt the latter approach in this work due to the ease with which it can be implemented.

The local direct stability problem for the *local* eigenvector $\hat{q}(y)$ [see Eq. (20)] is solved using the pseudospectral collocation technique [35]. Collocation points in physical space, $y \in [-1,1]$, are mapped onto Chebyshev collocation points in the computational space, $\eta \in [-1,1]$. A mapping function suggested by Bayliss *et al.* [36] is used to resolve the base flow density gradient (see Fig. 4) over 12 to 14 points at all streamwise locations for each of the cases analyzed in this paper. This yields a generalized matrix eigenvalue problem for the local eigenvalues ω and the local discrete eigenvector $\hat{q}_d$ as follows:

$$\mathbf{A}\hat{q}_d = -i\omega\mathbf{B}\hat{q}_d, \tag{22}$$

where the matrix $\mathbf{A}$ represents the discretized form of the local LNS operator which depends on the spatial wave number, k. We use the implementation of the QZ algorithm provided by the MATLAB "eig" function to solve the local eigenvalue problem given by Eq. (22), using a total of 70 collocation points for all computations in this paper. This is found to be sufficient to ensure that the maximum absolute change in the eigenvectors, with further increase in number of collocation points, is less than 1% for all cases. The $\hat{q}_d$ at each x location is normalized with the value of the $\hat{v}$ component at $y = -0.1$.

We solve the local spatiotemporal problem to determine the local absolute frequency ω_o at each streamwise location, using the saddle-point search algorithm of Deissler [37], in conjunction with Eq. (22). Two saddle points are found at each streamwise location, corresponding to pinching between local $k^{\pm}$ branches for all cases. Both of these saddle point series are continued into the complex x

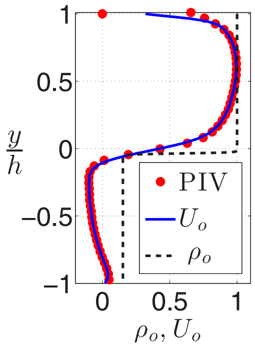

FIG. 4. Typical base flow velocity and density profiles ($\phi = 0.72$, $x = 0.26$). Time-averaged velocity data (symbols) from experiments (Ref. [19]) are overlaid for comparison. The density profile width is from the baseline estimate.

plane using rational polynomial fits of the form $p^m(x)/q^m(x)$ [31,38]. The value of m is varied between 5 and 30 for each series until the saddle point location (x_s) and $\omega_s = \omega_o(x_s)$ converges. We use the same approach as in the spatiotemporal analysis, albeit using the converged rational fit for $\omega_o(x)$ for each series, to find the corresponding ω_s values from initial estimates. In each case, ω_g is determined from the ω_s values for the two saddle point series, as the one that is higher in the complex ω_o plane, following the arguments of Pier and Peake [34]. The corresponding $x_g = x_s$ now gives the location of the saddle point on the complex x plane. The value of $\mathrm{Im}(\omega_g)$ for all cases was found to be lesser than the maximum value of $\mathrm{Im}[\omega_o(x)]$ on the real x axis corresponding to the $\omega_o(x)$ series that does not determine ω_g. Thus, the global mode structure is determined by the local stability solutions corresponding to the two spatial $k^{\pm}$ branches for ω_g that connect at x_g in the complex X plane and can therefore be constructed using the corresponding $\hat{q}_d$ [20].

The local discrete adjoint eigenvector, $\hat{q}_d^{\dagger}$, needed to construct the adjoint global mode using Eq. (21), is determined using the direct adjoint approach. The continuous inner product given in Eq. (12) is discretized, yielding $\langle q_{1d}, q_{2d}\rangle = q_{1d}^H \mathbf{M} q_{2d}$, where the superscript "H" denotes the transpose conjugate and $\mathbf{M}$ is a diagonal matrix generated by the application of the trapezoidal rule for a nonuniform mesh in physical space to Eq. (12). The matrices corresponding to the discrete adjoint problem are given by $\mathbf{A}^{\dagger} = \mathbf{M}^{-1}\mathbf{A}^{\mathbf{H}}\mathbf{M}$ and $\mathbf{B}^{\dagger} = \mathbf{M}^{-1}\mathbf{B}^{\mathbf{H}}\mathbf{M}$. The nullspace of $\mathbf{A}^{\dagger} - \omega_g^* \mathbf{B}^{\dagger}$ gives the vector $\hat{q}_d^{\dagger}$ [20]. We use the "null" function provided by MATLAB to evaluate the $\hat{q}_d^{\dagger}$ vectors.

We also define the following measure to characterize the intensity of flow velocity fluctuations due to the global mode at a given streamwise location,

$$e(x) = \int_{-1}^{1} (|\tilde{u}(x,y)|^2 + |\tilde{v}(x,y)|^2)dy. \tag{23}$$

The integral in Eq. (23) is evaluated using Gauss-Chebyshev quadrature.

B. Base flow

The instantaneous velocity fields determined from PIV measurements described in Hong *et al.* [19] for the $\phi = 0.63$, 0.72, and 0.85 cases are time averaged and smoothed at each x using a three point moving average filter along the y direction. Profiles of $U_o(y)$ at each x are then determined by fitting smooth piecewise splines through the data using the "fit" routine provided by MATLAB.

The density field in each case is determined using the raw instantaneous PIV images as follows. First, the boundary between unburnt and burnt gas in each PIV image is identified from tracking the edge of the high-seed particle density region corresponding to the unburnt gas as described in

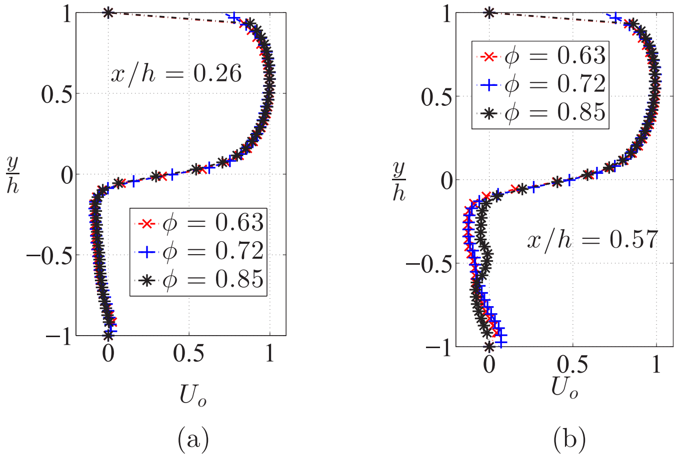

FIG. 5. Time-averaged axial base flow velocity profiles at (a) $x/h = 0.26$ and (b) $x/h = 0.57$, measured using PIV by Hong *et al.* [19].

Hong *et al.* [18]. The time-averaged location of the density gradient, y_f, and the root-mean-square variation of the density gradient position about the mean, δ_f, are evaluated as a function of streamwise coordinate x, using the edges extracted from each instantaneous image. Between 500 and 530 edges were used to determine y_f and δ_f, for all cases. The base flow gas density profile is then determined by fitting a hyperbolic tangent profile between burnt and unburnt gas density using y_f and δ_f as follows,

$$\rho_o(y) = 1 + \frac{r}{2}\left[1 - \tanh\left(\frac{y - y_f}{\delta_f}\right)\right], \tag{24}$$

where r is the ratio of density between burnt and unburnt gases. This is determined for each dataset from the adiabatic flame temperature for the value of ϕ corresponding to the dataset, using the GASEQ program [39].

Base flow profiles for density and velocity from the data are extracted from $x = 0.1$ up to the streamwise location where the uncertainty in the estimate of y_f was 10% of the same with 99% confidence. We found that this was sufficient to resolve the spatial structure of the adjoint modes near the step and hence draw conclusions about flow receptivity for all cases. Moreover, Hong *et al.* [18] report an uncertainty of ∼0.14 mm in locating the edge between high and low seed particle density regions. This uncertainty translates to a spatially varying uncertainty between 10%–20% in determining δ_f across all cases. We account for this in our analysis by repeating the local stability analyses at each streamwise location for both baseline δ_f as well as for $1.2\delta_f$ (i.e., 20% larger) to estimate the bounds on ω_g for the present data. Figure 4 shows typical velocity and density profiles obtained from the fitting procedure for $\phi = 0.72$ and $x = 0.26$. The PIV data from velocity measurements have been overlaid on these fits for comparison.

Figures 5(a) and 5(b) show time-averaged axial flow velocity profiles at two streamwise locations corresponding to $x = 0.26$ [Fig. 5(a)] and $x = 0.57$ [Fig. 5(b)] downstream of the step. Note that these fits show regions of forward and revese flow connected across a shear layer. This structure is similar to the model profiles used in prior local stability analysis studies [9,24]. Also, the velocity profiles for $\phi = 0.63$ and 0.72 cases are nearly identical at both locations shown in Fig. 5 as well as other streamwise locations considered in this study. The profile corresponding to the $\phi = 0.85$ case, however, shows a significantly different variation of the reverse flow velocity from the other two cases at $x = 0.57$ [see Fig. 5(b)]. The reason for this may be attributed to the movement of the nominal flame stabilization location towards the step resulting in a change in the time-averaged structure of the recirculation zone with increasing ϕ, as discussed in Hong *et al.* [19]. The effect of this change

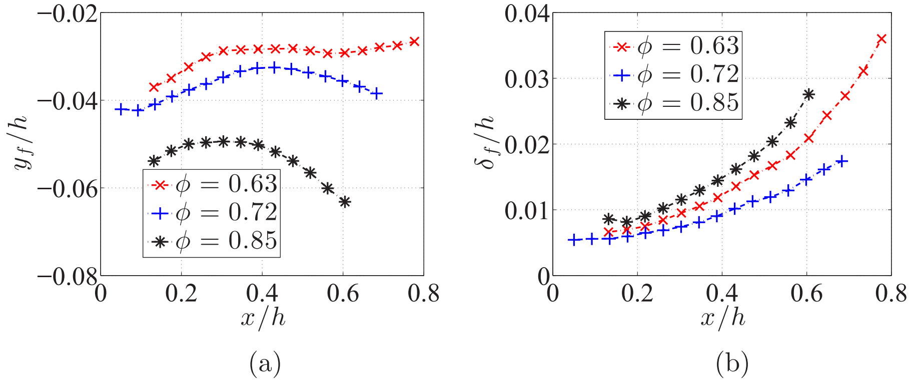

FIG. 6. Variation of density base flow profile parameters (a) y_f and (b) δ_f, determined using seeding density change edges determined from raw PIV data (Ref. [19]).

in flame flame stabilization location can be seen in the values of δ_f and y_f that characterize the time-averaged density profile [see Eq. (24)]. Figures 6(a) and 6(b) show the variation of y_f and δ_f with streamwise distance for the three values of ϕ considered in this study. Note that for $\phi = 0.85$, the density profile is located at a greater depth from the edge of the step into the recirculation zone than for the $\phi = 0.63$ and 0.72 cases [see Fig. 6(a)] and is nominally thicker [see Fig. 6(b)]. Further, these density profile parameters show that the density gradient is nominally contained within the shear layer behind the step at all streamwise locations and ϕ values considered in the present study. Thus, from prior studies [9,24] the local absolute/convective nature of the the flow profiles can be expected to be very sensitive to changes in the density profile shape. This in turn suggests that a change in flame stabilization location downstream of the step can cause the flow to change its *global* stability characteristics from being self-excited to being stable or vice versa [29].

V. RESULTS

Figure 7 shows a typical result from a local temporal stability analysis for the base flow profiles at $x = 0.26$ for the $\phi = 0.63$ case ($k = 3\pi$). The shear layer mode is marked by a red circle in

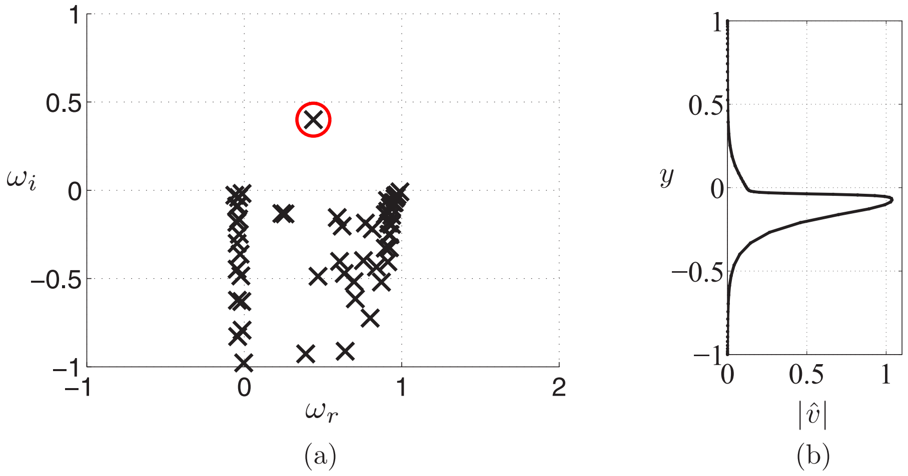

FIG. 7. Typical result from local stability analysis ($\phi = 0.63$, $k = 3\pi$, $x = 0.26$) (a) eigenvalue spectrum with the shear layer mode encircled and (b) $\hat{v}$ eigenvector corresponding to the shear layer mode.

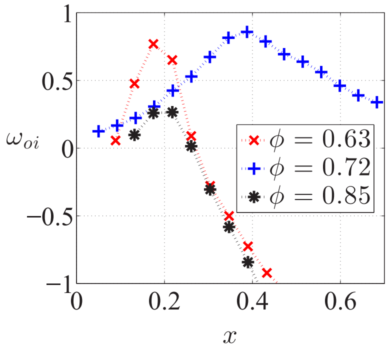

FIG. 8. Variation of local absolute growth rate for the shear layer mode along the streamwise direction for the saddle point series that determines the complex global frequency.

Fig. 7(a). Figure 7(b) shows the corresponding $|\hat{v}|$ profile which shows that the magnitude of the unsteady velocity fluctuations due to this mode is large in the region where the shear layer behind the step is located. The factors influencing the local temporal instability characteristics as well as the local absolute/convective instability characteristics of this mode have been discussed in a prior paper [9]. Figure 8 shows the variation of the growth rate of the impulse response, ω_{oi}, for the three values of ϕ considered in this paper. A pocket of local absolute instability [i.e., Im(ω_o) > 0] is seen for the $\phi = 0.63$ case for $0.1 < x < 0.3$. The width of this local absolute instability pocket expands along the streamwise direction for $\phi = 0.72$, with the peak local absolute growth rate being comparable to that of the $\phi = 0.63$ case. The width of the locally absolutely unstable region for $\phi = 0.85$ shrinks again to be about the same width as that for $\phi = 0.63$, albeit with a growth rate that is smaller by a factor of 3. Also, for both $\phi = 0.63$ and 0.85 cases, the flow is convectively unstable for $x > 0.3$.

Figures 9(a)–9(c) show the spatial variation of the instantaneous snapshot for the v' field due to the global shear layer mode, determined using Eq. (20). In all cases, a typical length scale (in terms of step height) of the structures appearing in the mode is ~0.4 for $\phi = 0.63$ and ~0.6 for $\phi = 0.72$ and 0.85. The length scale over which the base flow varies can be estimated as the length of the recirculation zone behind the step, which varies monotonically from ~5.5 ($\phi = 0.63$) to ~3 ($\phi = 0.85$) [19]. Thus, the ratio of these length scales is ~0.2 or less for the three cases analyzed here. This justifies the use of the WKBJ based approach for reconstructing global modes in the

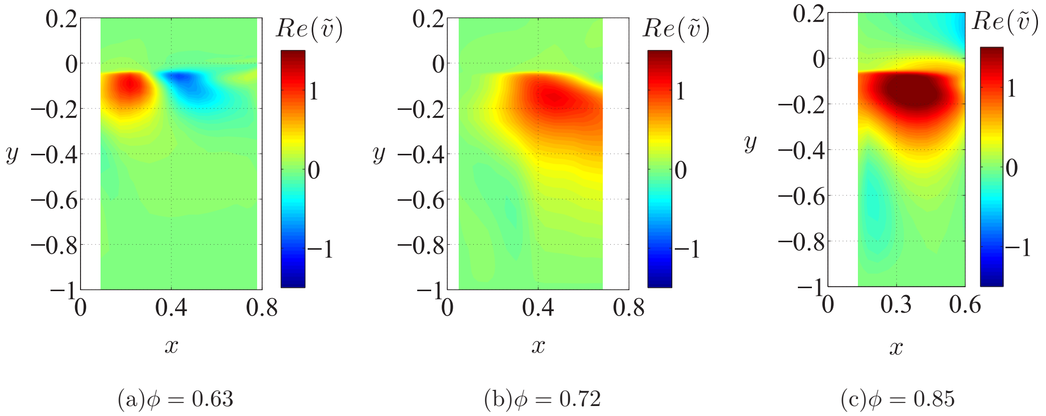

(a) $\phi = 0.63$ (b) $\phi = 0.72$ (c) $\phi = 0.85$

FIG. 9. Instantaneous v'-velocity component of the global shear layer mode for (a) $\phi = 0.63$ (b) $\phi = 0.72$ and (c) $\phi = 0.85$.

TABLE I. Global complex hydrodynamic stability analysis results for the shear layer mode determined from short combustor data. The columns list ϕ, ω_g, ω_g, respectively, assuming a 20% larger value of δ_f, the range over which the global frequency (f_g) changes due to the uncertainty in the value of δ_f and the combustion instability state observed in the long combustor at the corresponding condition. The fundamental acoustic eigenfrequency of the long combustor is 40 Hz [21].

ϕ	ω_g	$\omega_{g,1.2\delta_f}$	f_g (Hz)	Combustion instability state
0.63	$1.88 + 0.72i$	$2.88 + 0.37i$	85–131	Mode I
0.72	$0.93 + 0.66i$	$0.99 + 0.85i$	42–45	Mode II
0.85	$2.30 + 0.21i$	$2.70 + 0.005i$	104–122	Mode III

present study. The results for ω_g for each of the above global modes are summarized in Table I. The first column lists the equivalence ratio. The second column lists ω_g as determined from the local spatiotemporal analysis results for the baseline value of local density profile thickness (δ_f). The third column lists $\omega_{g,1.2\delta_f}$, i.e., ω_g determined by increasing the density layer thickness by 20% to account for the effect of uncertainty in detecting the instantaneous location of the edge between cold and hot gas in the raw PIV images as discussed earlier. The last column lists the range over which the oscillation frequency of the mode, f_g, varies for a 20% variation in δ_f.

Prior studies have shown that estimates of ω_g obtained by making the weakly nonparallel base flow assumption, tend to overestimate the value of $\mathrm{Im}(\omega_g)$ when compared with the value for the same determined from the fully two-dimensional stability methods for wakes [20,31]. Thus, the values of ω_{gi} given in Table I show that given the uncertainty in δ_f, the shear layer mode is globally unstable for the $\phi = 0.63$ and 0.72 cases. The $\phi = 0.85$ is stable or at best marginally unstable, within the limits of uncertainty in the experimental data, since $\mathrm{Im}(\omega_{g,1.2\delta_f}) \sim 0$. Note that these results have been determined for base flows taken from the short combustor experiments that do not show coherent acoustic pressure oscillations at these values of ϕ. As such, the frequencies mentioned in Table I correspond to the hydrodynamic instability of the shear layer. Figure 10 shows the streamwise variation of the intensity of flow oscillations [$e(x)$, see Eq. (23)] determined from the variation of $\tilde{u}$ and $\tilde{v}$ of the shear layer mode for each of the three cases. The curves in each case have been normalized by their values at $x = 0.17$. The $\phi = 0.72$ case shows the highest rate of spatial growth of flow oscillation intensity along the streamwise direction, due to the self-excited shear layer mode. We next discuss the implications of the results in Table I regarding which mechanism sustains the hydrodynamic flow velocity oscillations that in turn drive the heat-release oscillations responsible for sustained pressure oscillations in the long combustor experiments of Hong *et al.* [18].

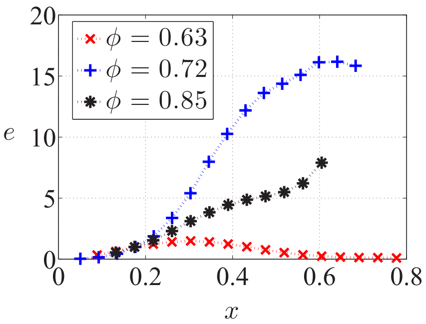

FIG. 10. Variation of the intensity of velocity fluctuations along the streamwise direction. The curves have been normalized by their value at $x = 0.17$.

Consider first the $\phi = 0.63$ case for which the shear layer oscillation frequency (f_g) range is predicted as 85–131 Hz (see Table I). This range of frequencies is very different from the fundamental *acoustic* eigenfrequency of the long combustor, $f_a \sim 40$ Hz, determined from a quasi-1D acoustic network analysis—see Ref. [21] for detail. This suggests that any heat-release oscillations that the shear layer induces would be strongly nonresonant. Further, Fig. 10 shows that the spatial growth rate of velocity oscillations due to the shear layer mode at $\phi = 0.63$ is very small and decays very quickly with distance downstream of the step where the flame sheet is located. These two results suggest that at $\phi = 0.63$, the self-excited shear layer oscillations do not induce coherent heat-release oscillations in the combustor through the semi-open loop mechanism. Further, even though the shear layer is self-excited, the large difference between f_a and f_g suggests that the receptivity of the shear layer mode to forcing at f_a, which is inversely proportional to this frequency difference [see Eq. (19)], is small. Therefore, it is unlikely that synchronization of the shear layer oscillation can occur, with low amplitude acoustic velocity oscillations due to the combustion noise generated by background turbulence at f_a. For all these reasons, the long combustor remains quiescent at the $\phi = 0.63$ operating condition.

Consider next the $\phi = 0.72$ case, where low-amplitude coherent pressure oscillations coupled with a coherently wrinkled flame attached near the step, and were observed in the long combustor experiments [18]. Table I shows that $f_g \sim 42$ Hz for $\phi = 0.72$, which closely matches f_a. Figure 10 shows that the resulting shear layer oscillations grow with downstream distance, accounting for the observation of coherent flame wrinkling in the experiment. Hong *et al.* [21] report experimental measurements of the phase difference between heat-release and pressure oscillations in the long combustor experiments for various operating conditions. Their results show that for $0.68 < \phi < 0.8$, the oscillating pressure leads the oscillating heat-release rate by ~90°. This suggests that the heat-release oscillation associated with the flame wrinkling generated by the self-excited shear layer mode, does not optimally force the acoustic pressure field. Therefore, acoustic damping in the combustor causes the pressure amplitude in the combustor to saturate at values lower than those observed in the Mode III state (see Fig. 3). Table I shows that as ϕ departs from $\phi = 0.72$, the value of f_g departs from 42 Hz. Therefore, this suggests that the resulting heat-release oscillations become nonresonant, resulting in a reduction in the amplitude of acoustic pressure oscillations, as shown in Fig. 3 for the long combustor. Thus, from all of these observations, we conclude that the pressure oscillations in the Mode II state of combustion instability in the long combustor are essentially driven by heat-release oscillations generated by semi-open loop forcing of the flame sheet by the self-excited shear layer mode. The fact that the overall acoustic amplitude is low suggests that the shear layer oscillations did not synchronize with the acoustic velocity oscillations, even for the near resonant $\phi = 0.72$ case. Investigating further as to why this is the case will require further nonlinear analysis, which is beyond the scope of this paper.

Finally, consider the results from the present hydrodynamic stability analysis for the $\phi = 0.85$ case shown in Table I for which the shear layer mode is stable or at best marginally unstable for this value of ϕ. This suggests that the shear layer mode responds strongly to acoustic velocity forcing imposed on it, resulting in strong spatial growth of hydrodynamic velocity oscillations as Fig. 10 shows. Further, Figs. 11(a) and 11(b) show the spatial variation of $|\tilde{u}^\dagger|$ and $|\tilde{v}^\dagger|$ for the $\phi = 0.85$ case, showing that the shear layer mode is strongly receptive to velocity forcing at the step. Therefore, given that the step nominally corresponds to the location of an acoustic velocity antinode in the combustor, strong coupling between the hydrodynamic shear layer mode and the acoustic forcing results, causing the shear layer to roll up. The results from Hong *et al.* [21] show that the acoustic pressure-heat-release oscillation phase difference varies between 0° and 45° for $\phi > 0.8$. This suggests optimal forcing of the acoustic field by heat-release oscillations, thereby resulting in higher values of acoustic amplitude for $\phi > 0.8$ as Fig. 3 shows. All of these facts suggest that heat-release oscillations for the Mode III state are driven by the fully coupled mechanism [see Fig. 1(b)] due to the shear layer in the long combustor being forced by the acoustic velocity oscillations. Interestingly, Fig. 3 shows that the short combustor also shows coherent pressure oscillations at its fundamental acoustic eigenfrequency for $\phi > 0.85$ [19]. This similarity between the value of ϕ at which both combustors show the onset of

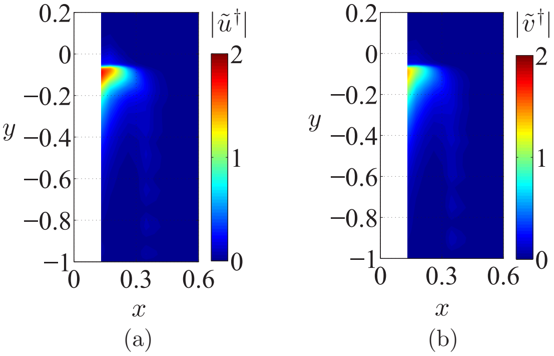

FIG. 11. Spatial variation of (a) $|\tilde{u}^\dagger|$ and (b) $|\tilde{v}^\dagger|$ for $\phi = 0.85$. The step edge is at $(x, y) = (0,0)$.

pressure oscillations suggests that the shear layer is forced by acoustic velocity oscillations at their corresponding fundamental eigenfrequencies. The relatively low OASPL in the short case when compared to the long is due to increase in the fundamental acoustic eigenfrequency and hence increased acoustic damping, due to the reduced combustor length.

We emphasize that the terms “semi-open loop” and “fully coupled” introduced in this paper refer to differences in the way hydrodynamic velocity oscillations are generated in the combustor. As discussed in the preceding paragraphs, the generation of heat-release oscillations by these velocity oscillations due to either mechanism does not guarantee the emergence of sustained pressure oscillations in combustors. The latter depends on whether the phase difference between the heat-release oscillations and acoustic pressure oscillations causes them to grow, i.e., the Rayleigh criterion for growth of pressure oscillations must be satisfied [40]. This critically depends on the characteristics of the heat-release oscillations generated by the hydrodynamic instability. Prior work on the heat-release response transfer functions of premixed flames excited by velocity oscillations [2,3] have shown that the characteristics of these transfer functions are very sensitive to the characteristics of the underlying unsteady velocity field, e.g., the phase speed of velocity oscillations [3]. Thus, the results of Hong *et al.* [18] suggest that the mere presence or absence of a self-excited hydrodynamic mode with a frequency matching those of the combustor acoustic eigenmodes is insufficient to conclude that high amplitude pressure oscillations will result. Clarifying this point will require an extension of the theoretical analysis presented in this paper to includes acoustic oscillations within the analysis framework. The recent work of Magri *et al.* makes a good beginning toward these types of analysis [41]. Nevertheless, the analyses presented in this paper, applied to experimental data, highlight the two mechanisms by which hydrodynamic instabilities may drive thermoacoustic instabilities in combustors.

We next discuss the results of the backward-facing step experiments of Charkarvarthy *et al.* [23] in the context of the present results. They investigated combustion instability state transitions in a nonpremixed backward-facing step combustor using methane as fuel. Experiments were performed by varying inflow air velocity while holding the fuel mass flow rate constant. The variation of the peak acoustic pressure oscillation amplitude as well as the frequency at which this occurs (instability frequency), for inflow velocities varied between ∼3–30 ms^{-1} were reported at two fuel mass flow rates: $\dot{m}_f = 0.065\ \text{kgs}^{-1}$ and $\dot{m}_f = 0.316\ \text{kgs}^{-1}$. For both cases, the results show that instability frequency initially remained constant up to ∼14 ms^{-1} for $\dot{m}_f = 0.065\ \text{kgs}^{-1}$ and ∼22 ms^{-1} for $\dot{m}_f = 0.316\ \text{kgs}^{-1}$. With further increase in air velocity, the instability frequency varied linearly with velocity for both cases. Also, the instability frequency for both $\dot{m}_f$ cases was found to be insensitive to the total length of the combsutor, even when the total combustor length is halved. Time-resolved CH* chemiluminescence imaging of the flame showed that the flame shows strong rollup due to vortical structures being generated downstream of the step [23]. This suggests that the heat-release oscillations in their combustor are being driven by self-excited hydrodynamic modes, i.e., through the semi-open loop forcing mechanism. However, a quantitative estimate of hydrodynamic instability frequencies and acoustic eigenfrequencies for their combustor is not possible due to the lack of companion base flow measurements for their experiment.

VI. CONCLUSION

Flows in gas turbine combustors are composed of several features such as shear layers and recirculation zones. These features can cause these flows to become unsteady due to self-excited hydrodynamic instability. Hydrodynamic modes can also be stable but receptive to velocity disturbances imposed by acoustic waves. The resulting velocity oscillations couple with the premixed flame sheet and produce heat-release oscillations. When self-excited hydrodynamic modes have natural oscillation frequencies close to (but not necessarily equal to) a combustor acoustic eigenmode, the feedback from the acoustic mode is not necessary for sustaining heat-release oscillations. Combustion instability is sustained if these heat-release oscillations couple favorably with the acoustic pressure field. We call this the semi-open loop mechanism of acoustic-hydrodynamic coupling. Globally stable hydrodynamic modes can be *locally* convectively unstable and thus give rise to large hydrodynamic velocity fluctuations, when forced by the acoustic velocity fluctuations. These velocity fluctuations couple with the flame sheet resulting in heat-release oscillations. The latter can drive the hydrodynamic mode through the acoustic velocity oscillations they generate, resulting in a feedback loop. We call this the fully closed-loop mechanism of acoustic-hydrodynamic coupling.

This paper shows evidence for these two types of coupling mechanisms in the “long” [18] and “short” [19] premixed backward-facing step combustor experiments of Ghoniem and coworkers. The combustors are identical in both sets of experiments, except for the length of the duct downstream of the step. The mixture equivalence ratio (ϕ) is varied in both sets of experiments from the lean-blow out (LBO) limit to the stoichiometric limit. The long combustor shows two unsteady combustion instability states characterized by coherent acoustic pressure fluctuations of low amplitudes (designated as “Mode II” [18]) and high amplitudes (designated as “Mode III” [18]). These states are also characterized by qualitatively different unsteady flame behavior. The short combustor is observed to be quiescent for all these operating conditions. A global hydrodynamic stability analysis is performed using time-averaged flow fields, determined from the PIV measurements in the quiescent, “short” combustor burning propane and air for $\phi = 0.63, 0.72$ and 0.85. We find that the first two cases are hydrodynamically globally self-excited while the third case is hydrodynamically stable but receptive to velocity forcing near the step. This suggests that acoustic pressure oscillations in the Mode II state in the long combustor are driven primarily by the semi-open loop forcing mechanism, while the Mode III state is sustained by the fully coupled forcing mechanism.

These results suggest that the proximity of the combustor acoustic eigenfrequencies and hydrodynamic eigenfrequencies are the key factor controlling the effectiveness of coupling between acoustic velocity oscillations and hydrodynamic modes. Stabilizing self-excited hydrodynamic modes by changing the combustor geometry to change the characteristics of the base flow field would result in a change in the oscillation frequency of the hydrodynamic mode. This can help mitigate combustion instability driven by semi-open loop forcing. Further, the receptivity analysis presented in this paper can be applied to stable modes to ascertain regions where these modes are receptive to forcing. This analysis can help make configurational changes to combustors that would spatially misalign the regions of high receptivity and high acoustic mode amplitudes, thereby mitigating the influence of the fully coupled mechanism of acoustic-hydrodynamic mode interactions in causing velocity oscillations. Also, knowing where the combustor hydrodynamic modes are receptive can guide placement of actuators for active control in the combustor, for maximum control effectiveness.

Finally, the present paper uses base flows determined from experiments within its analysis framework. This is potentially problematic in the industrial setting where it may be challenging to gain optical access to make similar measurements or may even be impossible if combustor prototypes have not been built. However, the analysis methods presented in this paper can be applied directly to base flows determined from computational methods such as large eddy simulations or unsteady Reynolds-averaged Navier-Stokes simulations of combustor flows. This would allow for an assessment of the susceptibility of combustor configurations to combustion instability at various operating conditions of interest during early stages of the combustor design process.

[1] T. C. Lieuwen, *Unsteady Combustor Physics* (Cambridge University Press, Cambridge, 2012).
[2] T. Schuller, D. Durox, and S. Candel, A unified model for the prediction of laminar flame transfer functions: Comparisons between conical and v-flame dynamics, Combust. Flame **134**, 21 (2003).
[3] Preetham, S. Hemchandra, and T. Lieuwen, Dynamics of laminar premixed flames forced by harmonic velocity disturbances, J. Propul. Power **24**, 1390 (2008).
[4] S. Schlimpert, S. Hemchandra, M. Meinke, and W. Schröder, Hydrodynamic instability and shear layer effect on the response of an acoustically excited laminar premixed flame, Combust. Flame **162**, 345 (2015).
[5] K. Kashinath, S. Hemchandra, and M. P. Juniper, Nonlinear phenomena in thermoacoustic systems with premixed flames, J. Eng. Gas Turbines Power **135**, 061502 (2013).
[6] K. Kashinath, S. Hemchandra, and M. P. Juniper, Nonlinear thermoacoustics of ducted premixed flames: The influence of perturbation convection speed, Combust. Flame **160**, 2856 (2013).
[7] J.-M. Chomaz, P. Huerre, and L. G. Redekopp, A frequency selection criterion in spatially developing flows, Stud. Appl. Math. **84**, 119 (1991).
[8] P. A. Monkewitz, P. Huerre, and J.-M. Chomaz, Global linear stability analysis of weakly nonparallel shear flows, J. Fluid Mech. **251**, 1 (1993).
[9] K. Manoharan and S. Hemchandra, Absolute/convective instability transition in a backward facing step combustor: Fundamental mechanism and influence of density gradient, J. Eng. Gas Turbines Power **137**, 021501 (2015).
[10] K. Manoharan, S. Hansford, J. O' Connor, and S. Hemchandra, Instability mechanism in a swirl flow combustor: Precession of vortex core and influence of density gradient, in *Proceedings of the ASME Turbo Expo 2015: Turbine Technical Conference and Exposition, paper no. GT2015-42985* (American Society of Mechanical Engineers, New York, 2015).
[11] K. Oberleithner, S. Terhaar, L. Rukes, and C. O. Paschereit, Why nonuniform density suppresses the precessing vortex core, J. Eng. Gas Turbines Power **135**, 121506 (2013).
[12] B. Emerson, J. O' Connor, M. Juniper, and T. Lieuwen, Density ratio effects on reacting bluff-body flow field characteristics, J. Fluid Mech. **706**, 219 (2012).
[13] M.-H. Yu and P. A. Monkewitz, The effect of nonuniform density on the absolute instability of two-dimensional inertial jets and wakes, Phys. Fluids A **2**, 1175 (1990).
[14] U. A. Qadri, G. J. Chandler, and M. P. Juniper, Self-sustained hydrodynamic oscillations in lifted jet diffusion flames: Origin and control, J. Fluid Mech. **775**, 201 (2015).
[15] S. Terhaar, K. Oberleithner, and C. O. Paschereit, Key parameters governing the precessing vortex core in reacting flows: An experimental and analytical study, Proc. Combust. Inst. **35**, 3347 (2015).
[16] T. J. Poinsot, A. C. Trouve, D. P. Veynante, S. M. Candel, and E. J. Esposito, Vortex-driven acoustically coupled combustion instabilities, J. Fluid Mech. **177**, 265 (1987).
[17] K. C. Schadow and E. Gutmark, Combustion instability related to vortex shedding in dump combustors and their passive control, Prog. Energy Combust. Sci. **18**, 117 (1992).
[18] S. Hong, R. L. Speth, S. J. Shanbhogue, and A. F. Ghoniem, Examining flow-flame interaction and the characteristic stretch rate in vortex-driven combustion dynamics using PIV and numerical simulation, Combust. Flame **160**, 1381 (2013).
[19] S. Hong, S. J. Shanbhogue, and A. F. Ghoniem, Impact of fuel composition on the recirculation zone structure and its role in lean premixed flame anchoring, Proc. Combust. Inst. **35**, 1493 (2015).
[20] M. P. Juniper and B. Pier, The structural sensitivity of open shear flows calculated with a local stability analysis, Eur. J. Mech. B Fluids **49**, 426 (2015).

[21] S. Hong, S. J. Shanbhogue, R. L. Speth, and A. F. Ghoniem, On the phase between pressure and heat release fluctuations for propane/hydrogen flames and its role in mode transitions, Combust. Flame **160**, 2827 (2013).

[22] G. J. Chandler, M. P. Juniper, J. W. Nichols, and P. J. Schmid, Adjoint algorithms for the Navier-Stokes equations in the low mach number limit, J. Comput. Phys. **231**, 1900 (2012).

[23] S. R. Chakravarthy, O. J. Shreenivasan, B. Boehm, A. Dreizler, and J. Janicka, Experimental characterization of onset of acoustic instability in a nonpremixed half-dump combustor, J. Acoust. Soc. Am. **122**, 120 (2007).

[24] A. F. Ghoniem, A. Annaswamy, D. Wee, T. Yi, and S. Park, Shear flow driven combustion instability: Evidence, simulation and modeling, Proc. Combust. Inst. **29**, 53 (2002).

[25] A. H. Nayfeh, *Perturbation Methods* (John Wiley & Sons, New York, 2008).

[26] S. Mariappan and R. I. Sujith, Modelling nonlinear thermoacoustic instability in an electrically heated rijke tube, J. Fluid Mech. **680**, 511 (2011).

[27] J. P. Moeck, H. Schmidt, M. Oevermann, C. O. Paschereit, and R. Klein, An asymptotically motivated hyrodynamic-acoustic two-way coupling for modeling thermoacoustic instabilities in a Rijke tube, in *Proceedings of the 14th International Congress on Sound and Vibration (ICSV14)*, Vol. 978 (Curran Associates, Inc., New York, 2007), p. 7334.

[28] P. J. Schmid and D. S. Henningson, *Stability and Transition in Shear Flows*, Vol. 142 (Springer Verlag, Berlin, 2001).

[29] J.-M. Chomaz, Global instabilities in spatially developing flows: Nonnormality and nonlinearity, Annu. Rev. Fluid Mech. **37**, 357 (2005).

[30] D. G. Crighton and M. Gaster, Stability of slowly diverging jet flow, J. Fluid Mech. **77**, 397 (1976).

[31] M. P. Juniper, O. Tammisola, and F. Lundell, The local and global stability of confined planar wakes at intermediate Reynolds number, J. Fluid Mech. **686**, 218 (2011).

[32] K. Oberleithner, L. Rukes, and J. Soria, Mean flow stability analysis of oscillating jet experiments, J. Fluid Mech. **757**, 1 (2014).

[33] P. Huerre and P. A. Monkewitz, Absolute and convective instabilities in free shear layers, J. Fluid Mech. **159**, 151 (1985).

[34] B. Pier and N. Peake, Global modes with multiple saddle points, Eur. J. Mech. B Fluids **49**, 335 (2015).

[35] Edited by J. P. Boyd, *Chebyshev and Fourier Spectral Methods* (Dover Publications, Mineola, New York, 2000).

[36] A. Bayliss and E. Turkel, Mappings and accuracy for Chebyshev pseudospectral approximations, J. Comput. Phys. **101**, 349 (1992).

[37] R. J Deissler, The convective nature of instability in plane Poiseuille flow, Phys. Fluids **30**, 2303 (1987).

[38] A. J. Cooper and D. G. Crighton, Global modes and superdirective acoustic radiation in low-speed axisymmetric jets, Eur. J. Mech. B Fluids **19**, 559 (2000).

[39] C. Morley, Gaseq—A chemical equilibrium program for windows, http://www.gaseq.co.uk/

[40] Tim C. Lieuwen, *Unsteady Combustor Physics* (Cambridge University Press, Cambridge, 2012).

[41] L. Magri, Y.-C. See, O. Tammisola, M. Ihme, and M. P. Juniper, Multiple-scale thermo-acoustic stability analysis of a coaxial jet combustor, Proc. Combust. Inst. **36**, 3863 (2017).